

Imaging dendritic spines in the hippocampus of a living mouse by 3D-stimulated emission depletion microscopy

Stéphane Bancelin^{✉, a,*}, Luc Mercier,^a Johannes Roos^{✉, a},
Mohamed Belkadi,^a Thomas Pfeiffer,^a Sun Kwang Kim^{✉, b},
and U. Valentin Nägerl^{✉, a,*}

^aUniversity of Bordeaux, CNRS, Interdisciplinary Institute for Neuroscience, IINS,
UMR 5297, Bordeaux, France

^bKyung Hee University, Graduate School, Department of Science in Korean Medicine,
Seoul, Republic of Korea

Abstract

Significance: Stimulated emission depletion (STED) microscopy has been used to address a wide range of neurobiological questions in optically well-accessible samples, such as cell culture or brain slices. However, the application of STED to deeply embedded structures in the brain of living animals remains technically challenging.

Aim: In previous work, we established chronic STED imaging in the hippocampus *in vivo* but the gain in spatial resolution was restricted to the lateral plane. In our study, we report on extending the gain in STED resolution into the optical axis to visualize dendritic spines in the hippocampus *in vivo*.

Approach: Our approach is based on a spatial light modulator to shape the focal STED light intensity in all three dimensions and a conically shaped window that is compatible with an objective that has a long working distance and a high numerical aperture. We corrected distortions of the laser wavefront to optimize the shape of the bottle beam of the STED laser.

Results: We show how the new window design improves the STED point spread function and the spatial resolution using nanobeads. We then demonstrate the beneficial effects for 3D-STED microscopy of dendritic spines, visualized with an unprecedented level of detail in the hippocampus of a living mouse.

Conclusions: We present a methodology to improve the axial resolution for STED microscopy in the deeply embedded hippocampus *in vivo*, facilitating longitudinal studies of neuroanatomical plasticity at the nanoscale in a wide range of (patho-)physiological contexts.

© The Authors. Published by SPIE under a Creative Commons Attribution 4.0 International License. Distribution or reproduction of this work in whole or in part requires full attribution of the original publication, including its DOI. [DOI: [10.1117/1.NPh.10.4.044402](https://doi.org/10.1117/1.NPh.10.4.044402)]

Keywords: 3D-stimulated emission depletion; *in vivo* imaging; hippocampal window; point spread function optimization; super-resolution microscopy.

Paper 23006SSR received Feb. 7, 2023; revised manuscript received Mar. 31, 2023; accepted for publication Apr. 14, 2023; published online May 17, 2023.

1 Introduction

The hippocampus is a deeply embedded brain region, which plays a critical role in encoding new memories. In the hippocampus, as elsewhere in the mammalian brain, pyramidal neurons receive most of their excitatory synaptic input at dendritic spines, which are small protrusions in the postsynaptic membrane that house the postsynaptic signaling machinery including glutamate receptors. Structural and functional plasticity of dendritic spines is a fundamental neurobiological process that underlies all higher brain functions, such as memory, thought, and action,^{1,2} whereas spine dysfunction is closely associated with neuropsychiatric and neurodegenerative disorders, such as autism and Alzheimer's disease.³

*Address all correspondence to Stéphane Bancelin, stephane.bancelin@cnrs.fr; U. Valentin Nägerl, valentin.nagerl@u-bordeaux.fr

Two-photon fluorescence microscopy provides high depth penetration and optical sectioning in turbid media,⁴ making it the standard technique for imaging in acute brain slices^{5,6} and intact brains.⁷⁻⁹ Over the last 20 years, it has transformed our understanding of the structure and function of dendritic spines in mouse brain.¹⁰

Until now, most *in vivo* studies of dendritic spines have been limited to superficial layers of the cortex (somatosensory, motor, visual cortex),¹¹⁻¹³ mainly because of the challenge to optically reach more deeply embedded structures. For example, the hippocampus is more than 1 mm below the cortical surface of the mouse brain. Only a few groups have ventured into imaging hippocampal spines *in vivo*, relying either on surgical resection of the overlying cortex^{14,15} or a microendoscope with a gradient-index lens.¹⁶

However, 2-photon microscopy is a diffraction-limited approach, which offers at best a spatial resolution of around 350 nm laterally and 1 μm axially, falling substantially short of visualizing several key neuro-anatomical structures and spaces, including spine necks, axon shafts, astroglial processes, and synaptic clefts, whose sizes can range well below 100 nm. As a consequence, there is a great need to develop and improve super-resolution imaging techniques that could be applied to deeply embedded regions, such as the hippocampus. Among the various super-resolution methods, stimulated emission depletion (STED) microscopy¹⁷ is currently the only one that has been successfully applied *in vivo*,¹⁸⁻²² notably in the hippocampus.²³

STED microscopy is based on laser-scanning microscopy (such as confocal or 2-photon microscopy), where a Gaussian laser beam is focused to a small spot generating the fluorescence signal used to construct the image. In addition, there is a second laser (the STED laser), which exerts the opposite effect, namely it de-excites molecules by the process of stimulated emission. By spatially shaping the focal STED intensity like a donut,¹⁷ it is possible to suppress the spontaneous fluorescence in the peripheral region of the focal spot, narrowing down the effective point spread function (PSF) in the *XY* plane by up to an order of magnitude.²⁴ By delivering STED light also above and below the focal region (a profile referred to as “bottle beam”), it becomes possible to constrict the fluorescence along the optical axis as well.^{25,26}

In STED microscopy, spatial resolution and signal-to-noise ratio (SNR) of the images crucially depend on the quality of the PSF of the STED beam.²⁷ Yet, maintaining a high-quality PSF inside light scattering brain tissue poses several challenges. This problem is particularly evident in the context of *in vivo* imaging, where a variety of biological and mechanical constraints stand in the way of ensuring sufficiently good optical conditions for STED imaging. Notably, long working distance water immersion objectives typically used for *in vivo* imaging are not optimal for STED. Indeed, the effective STED resolution scales nonlinearly with the numerical aperture (NA) of the objective lens.²⁸ Hence, oil or glycerin immersion lens are typically preferred, offering high NA up to 1.49 at the expense of limited working distance. In addition to gain optical access to the brain, most studies rely on implanting a cranial window²⁹ in which a small part of the skull is replaced by a coverslip. Consequently, the mechanical stability of the cranial window attachment as well as of the brain itself are crucial, since any vibrations stemming from muscle contractions, pulmonary breathing, and blood pulsations can produce motion artefacts and diminish image quality.

The bottle beam PSF used for the axial gain in resolution is particularly sensitive to optical aberrations and misconfigurations in the beam path. Notably, the modified cranial window used to image the hippocampus^{15,24} reduced the effective NA, which prevented the use of a bottle beam profile for 3D-STED in our previous study based on a cylindrically shaped “hippocampal window.”²³ In this paper, we propose the use of a conically shaped window, specifically designed to maintain the bottle beam profile, while minimizing the size of the surgical resection of the overlying cortex.

2 Material and Methods

2.1 2-Photon STED Microscope

Imaging was performed using a custom-built upright laser-scanning fluorescence microscope, as previously described.^{23,27,30} In brief, the 2-photon excitation beam (100 fs, 80 MHz, 900 nm) was provided by a femtosecond titanium:sapphire laser (Tsunami, Spectra-Physics), pumped by

a high power continuous wave diode pumped solid state laser (Millennia EV 15, Spectra-Physics), sent through a Pockels cell (302 RM, Conoptics) to control the excitation power. The STED beam (592 nm, 700 ps, 80 MHz) was provided by another pulsed laser (Katana 06 HP, NKT Photonics) whose power was adjustable using a half-wave plate and a polarization beam splitter. Both lasers were synchronized and temporally overlapped using commercial electronics (“Lock-to-clock,” Model 3930 and 3931, Spectra-Physics).

The STED beam was passed via a spatial light modulator (SLM) (3D module, Abberior Instruments) to modulate the wavefront in a way that a donut or bottle beam intensity distribution of the STED light is achieved in the focal plane. Half and quarter-wave plates ($\lambda/2$ and $\lambda/4$) were used to produce a left-handed circular polarization at the entrance pupil of the objective. Both 2-photon excitation and STED beams were combined using a long-pass dichroic mirror (DCSPXRUV—T700, AHF). Appropriate lens combinations were used to conjugate the SLM on a telecentric scanner (Yanus IV, TILL Photonics), which was then imaged on the back focal plane of the objective (CFI Apo NIR 60 \times W, NA 1.0, Nikon) mounted on a z-focusing piezo actuator (Pifoc 725.2CD, Physik Instrumente). This objective provided a working distance of 2.8 mm, sufficient to bridge the physical distance between the surface of the brain and the deeply embedded hippocampus, while still offering a relatively high NA conducive for high-resolution imaging.

The epifluorescence signal was descanned, separated from the incident beams using a long-pass dichroic mirror (580 DCXRUV, AHF) and detected by an avalanche photodiode (SPCM-AQRH-14-FC, Excelitas) with appropriate notch (594S-25, Semrock) and bandpass filters (680SP-25, 520-50, Semrock) along the emission path. Signal detection and hardware control were performed via a data acquisition card (PCIe-6259, National Instruments) and the Inspector software (Abberior Instruments).

To visualize and prealign the donut or bottle PSFs, a pellicle beam splitter (BP145B1, Thorlabs) was flipped into the beam path to detect the signal reflected by gold beads (150 nm Gold nanospheres, Sigma Aldrich) using a photomultiplier tube (MD963, Excelitas). In the following, 2D-STED, z-STED, and 3D-STED will refer to images acquired using a pure donut, a pure bottle beam or a combination of the two beams, respectively. Optical resolution was assessed by imaging fluorescent beads (yellow–green fluorescent beads, 40 or 170 nm in diameter, Invitrogen) immobilized on glass slides.

2.2 Animal Experimentation

We used adult female and male transgenic mice (Thy1 – $H^{tg/+}$, 3 to 12 months old) where a subset of hippocampal neurons was fluorescently labeled with YFP.³¹ Heterozygous mice were used with sparse yet robust cytosolic labeling well adapted for high contrast superresolution imaging. The mice were group-housed by gender at a 12/12 h light/dark cycles. All procedures were in accordance with the Directive 2010/63/EU of the European Parliament and approved by the Ethics Committee of Bordeaux under agreement number 8899.

2.3 Hippocampal Window Implantation

Chronic hippocampal windows were implanted as described previously^{14,15,23,32} to provide optical access to the *Stratum oriens* and *Stratum pyramidale* of the CA1 region of the hippocampus. In brief, mice were anesthetized with isoflurane (2%) and received intraperitoneal injections of analgesic (buprenorphine, 0.05 mg/kg) and anti-inflammatory drugs (dexamethasone, 0.2 mg/kg) to minimize brain swelling during the surgical procedure. The mouse scalp was shaved in the surgical region, and the mouse was placed into a stereotaxic frame with a heating pad. Lidocaine was locally applied prior to the removal of the skin and periosteum above the skull. A 3-mm-diameter craniotomy was performed above the right or left hemisphere using a dental drill (anteroposterior –2.2 mm; mediolateral +1.8 mm). The dura was carefully removed using fine forceps before aspirating the somatosensory cortex above the hippocampus using a vacuum pump connect to 29 G blunt needle. The overlying alveus was carefully peeled away to expose the surface of the hippocampus. A custom-made metal tube sealed with a coverslip (#1) on the bottom side (both 3 mm in diameter) was inserted into the craniotomy and tightly

fixed to the skull with acrylic glue. Since our objective lens does not have a correction collar, this coverslip offers a good compromise between the thick #1.5 H coverslip, necessitating strong correction of spherical aberration with the SLM, and the thin #0 coverslip, which can be too fragile for cranial window implantation. Once in place, the hippocampal window was fixed using ultraviolet light curable dental cement.

2.4 In Vivo Imaging

After the surgery, mice received analgesics for 2 days (buprenorphine, 0.05 mg/kg, intraperitoneal injection) and be allowed to recover for at least 4 weeks before starting imaging sessions. During these sessions, mice were anesthetized under 4% isoflurane prior to be transferred to a custom-made 3D printed tiltable frame, based on ear bars and nose fixations, incorporating a mask delivering 1.5% to 2% isoflurane at 0.2 L/ min O₂. The eyes were protected with ointment (bepanthen) and body temperature was maintained using a heating pad with anal probe. Imaging of CA1 pyramidal neurons was performed at 10 to 30 μm depth to avoid scare tissue at the surface while limiting optical aberrations steaming from the sample.^{19,27} Typical image size was 20 × 20 μm² in XY with a pixel size of 20 nm, z stacks typically extended over 4 μm with a z-step size of 100 nm. Images were acquired with a 20 μs pixel dwell time, whereas excitation and STED laser powers were in the range of 10 to 20 mW after the objective lens. With these acquisition settings, no signs of phototoxicity were visible.

3 PSF Computation

The PSF of the STED beam was calculated using vectorial diffraction theory by Richard and Wolf,^{33,34} which makes it possible to calculate the electromagnetic field (\mathbf{E}) in an arbitrary point P close to the focal region of a high NA (NA ≥ 0.7) objective, based on the Debye integral^{35,36}

$$\mathbf{E}(P) = -\frac{ikf}{2\pi} \iint_{\Omega} \frac{A(\mathbf{s})}{s_z} e^{iks \cdot \mathbf{R}} d s_x d s_y, \quad (1)$$

where k is the wavenumber, f the objective focal length, Ω the solid angle of the exit pupil from the focal spot, \mathbf{s} the unit vector along each ray from the objective pupil to the focal volume, $A(\mathbf{s})$ the complex amplitude of the incident laser beam after the objective and \mathbf{R} the position vector of point P(x, y, z).

Considering the geometry depicted in Fig. 1(a), the diffraction integral can be expressed, in spherical coordinates, as^{36,37}

$$\mathbf{E}(x, y, z) = C \int_0^\alpha \int_0^{2\pi} B(\theta, \varphi) \mathbf{P}(\theta, \varphi) e^{i(M(\theta, \varphi) + \Phi(\theta, \varphi))} e^{k_0 n_1 (x \cos \varphi \sin \theta_1 + y \sin \varphi \sin \theta_1)} e^{ik_0 n_3 z \cos \theta_3} e^{ik_0 (n_3 d \cos \theta_3 - n_1 (t+d) \cos \theta_1)} \sin \theta d\theta d\varphi, \quad (2)$$

where C is a constant, k_0 the wavenumber in the vacuum, $\alpha = \arcsin(\text{NA}/n)$ the marginal ray angle, n_1 and θ_1 the refractive indices and incident angle in the (1) immersion media, (2) the coverslip, and (3) the sample, respectively, d the depth in the sample, t the thickness of the coverslip, $B(\theta, \varphi)$ the amplitude profile of the incident beam, \mathbf{P} the polarization state of the electromagnetic field in the focal region, $M(\rho, \varphi)$ the phase profile of the input beam, corresponding in our case to the phase mask used to shape the STED beam, and $\Phi(\theta, \varphi)$ the wavefront distortion with respect to the Gaussian reference sphere, which describes the optical aberrations in the system. Note that the second and third exponential terms correspond to the aberrations induced along the optical path through the coverslip and the biological sample.³⁷

Although passing through an aplanatic objective, the incident plane wave transforms into a spherical wave converging to the focal point. Therefore, assuming a Gaussian profile of the input beam, the amplitude distribution after the objective can be expressed as

$$B(\theta, \varphi) = B_0 e^{-\frac{\rho^2}{w^2}} \sqrt{\cos \theta}, \quad (3)$$

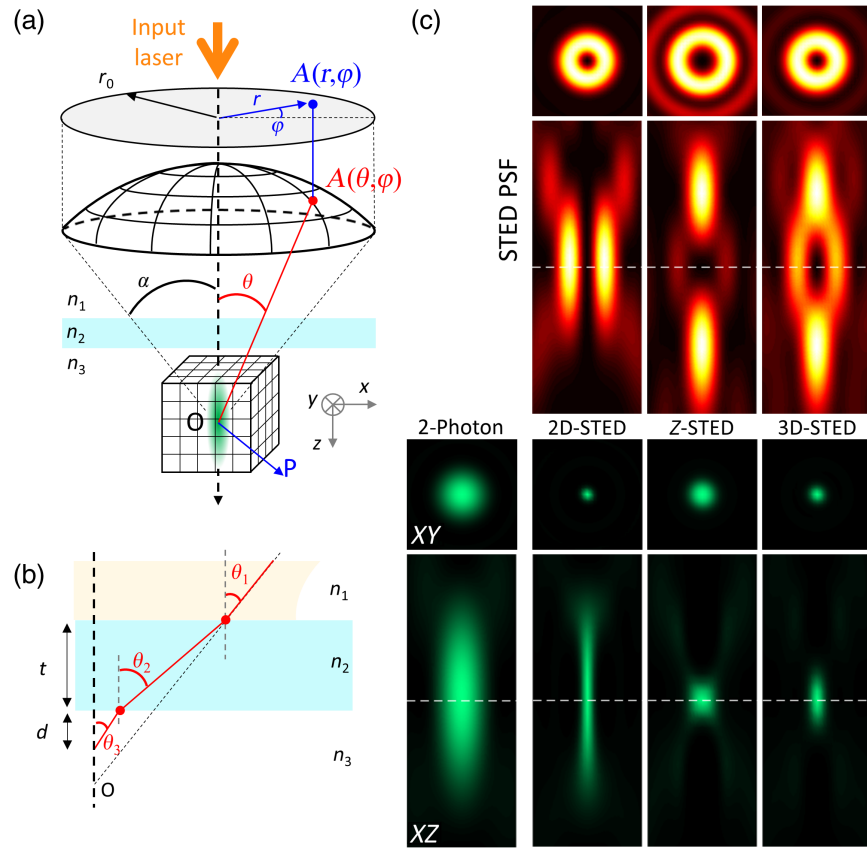


Fig. 1 (a) Schematic representation of the propagation of a light wave focused by a high NA objective used to calculate the PSF in the vicinity of the focus. (b) Refraction angles within the coverslip. Due to the refractive index mismatch, each interface decreases transmission and induces spherical aberrations. (c) STED beam (top, fire LUT) and effective fluorescence (bottom, green LUT) PSFs in XY plane (square panels, image size $1 \times 1 \mu\text{m}^2$) and XZ plane (rectangle panels, image size $1 \times 2.5 \mu\text{m}^2$), for the different configurations used in this paper (2-photon only, 2D-STED, z-STED and 3D-STED). The dashed line indicates the focus position.

where B_0 is a constant, w the beam waist, $\rho = f \sin \theta$ the cylindrical coordinate on the exit pupil of the objective lens, and $\sqrt{\cos \theta}$ the apodization term ensuring energy conservation while the beam pass through the objective. In addition, the objective transforms the input left-handed circular polarization $\mathbf{P}_0(\theta, \varphi) = (1, i, 0)$, classically used in STED microscopy, through tight focalization, which can be described as

$$\mathbf{P}(\theta, \varphi) = \mathcal{R}_\varphi^{-1} [\mathcal{P}^{(3)}]^{-1} \mathcal{I}^{(2)} \mathcal{P}^{(1)} \mathcal{L}_{\theta_1} \mathcal{R}_\theta \mathbf{P}_0, \quad (4)$$

where \mathcal{R}_φ is the rotation matrix around z axis, \mathcal{L}_θ describe the change in electric field as it passes through the objective, $\mathcal{P}^{(i)}$ corresponds to the coordinate system rotation in medium i , and $\mathcal{I}^{(2)}$ is the matrix describing the effect of the coverslip medium, considered as a stratified medium of two interfaces

$$\mathcal{R}_\varphi = \begin{pmatrix} \cos \varphi & \sin \varphi & 0 \\ -\sin \varphi & \cos \varphi & 0 \\ 0 & 0 & 1 \end{pmatrix}, \quad \mathcal{L}_\theta = \begin{pmatrix} \cos \theta & 0 & \sin \theta \\ 0 & 1 & 0 \\ -\sin \theta & 0 & \cos \theta \end{pmatrix}, \quad (5)$$

$$\mathcal{P}^{(l)} = \begin{pmatrix} \cos \theta_l & 0 & -\sin \theta_l \\ 0 & 1 & 0 \\ \sin \theta_l & 0 & \cos \theta_l \end{pmatrix}, \quad \mathcal{I}^{(2)} = \begin{pmatrix} T_p^{(2)} & 0 & 0 \\ 0 & T_s^{(2)} & 0 \\ 0 & 0 & T_p^{(2)} \end{pmatrix}, \quad (6)$$

where $T_{s,p}^{(2)}$ is the transmission coefficient in the coverslip (see³⁷ for complete derivation).

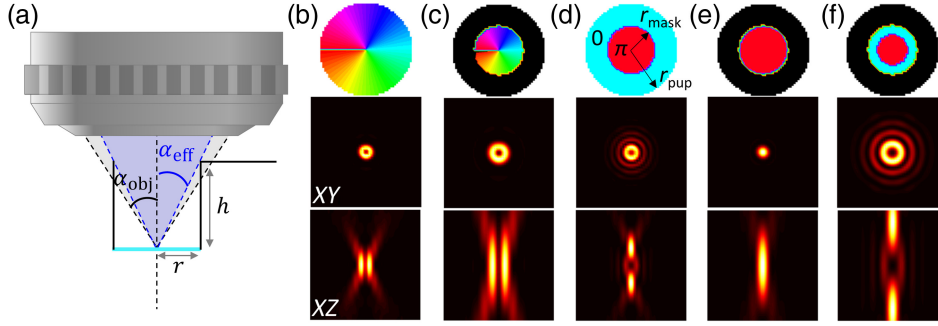


Fig. 2 (a) Schematic of the hippocampal cranial window and its effect on the focused beam, notably the clipping of the outer optic rays. Numerical simulation of the STED beam XY (middle panels) and XZ (bottom panels) profiles calculated for the different phase masks (top panels) used in STED microscopy: Donut (b) effective donut in presence of hippocampal window (c) bottle beam (d) effective bottle beam in presence of hippocampal window and (e) same with adjusted phase mask radius ($r_{\text{mask}} = 0.33r_{\text{pup}}$) enabling the retrieval of the (f) bottle profile. Image size: $5 \times 5 \mu\text{m}^2$.

Finally, in the case of left-handed circular polarization

$$\mathbf{P}(\theta, \varphi) = \begin{pmatrix} T_p^{(2)} \cos \theta_3 \cos^2 \varphi + T_s^{(2)} \sin^2 \varphi \\ T_p^{(2)} \cos \theta_3 \cos \varphi \sin \varphi - T_s^{(2)} \cos \varphi \sin \varphi \\ -T_p^{(2)} \sin \theta_3 \cos \varphi \end{pmatrix} + i \begin{pmatrix} T_p^{(2)} \cos \theta_3 \sin \varphi \cos \varphi - T_s^{(2)} \sin \varphi \cos \varphi \\ T_p^{(2)} \cos \theta_3 \sin^2 \varphi + T_s^{(2)} \cos^2 \varphi \\ -T_p^{(2)} \sin \theta_3 \cos \varphi \end{pmatrix}. \quad (7)$$

In the context of STED microscopy, the PSF of the STED beam is spatially shaped [Fig. 1(c)—top profiles] using specific phase masks $M(\theta, \varphi)$, that can be expressed as

$$M(\theta, \varphi) = \begin{cases} 0 & \text{No phase mask} & - & \text{Gaussian beam,} \\ \varphi & \text{Vortex phase mask} & - & \text{Donut beam,} \\ \begin{cases} \pi & \text{for } \theta \leq \theta_M \\ 0 & \text{for } \theta_M \leq \theta \leq \alpha \end{cases} & \text{Ring phase mask} & - & \text{Bottle beam,} \end{cases} \quad (8)$$

where $\theta_M = a \sin\left(\frac{r_{\text{mask}}}{r_{\text{pupil}}} \sin \alpha\right)$ is the angle between the optical axis and the ray passing through the edge of the π -phase ring of the phase mask of radius r_{mask} on the objective output pupil of radius r_{pupil} [Fig. 2(d)—top panel].

The focal intensity can be calculated as the squared modulus of the electric field

$$I = |\mathbf{E}|^2 = |E_x|^2 + |E_y|^2 + |E_z|^2. \quad (9)$$

Finally, the effective PSF [Fig. 1(c)—bottom profiles] is calculated as³⁸

$$I_{\text{eff}}(x, y, z) = I_{2P} e^{-\frac{\ln 2 I_{\text{STED}}}{I_{\text{sat}}}}, \quad (10)$$

where I_{exc} and I_{STED} are the excitation and STED beams, respectively, and I_{sat} is the saturation intensity, which describes the de-excitation rate of the molecules by the STED beam.

4 Results and Discussion

4.1 Impact of the Cranial Window

The chronic hippocampal window used here was originally developed to image pyramidal neurons in the hippocampus by 2-photon microscopy^{14,15,32} using a 0.8 NA objective. In this case, the specific geometry of the window, a metal cylinder sealed with a coverslip, limited the angle of the marginal rays transmitted through the window [Fig. 2(a)]. Indeed, to reach the hippocampus surface, the implanted cylinder and holder has a height (h) of 2.23 mm and an inner diameter (r) of 2.6 mm, which corresponds to a maximum opening angle of 30.2 deg and hence an effective NA of 0.67. Although such an NA can be acceptable for 2-photon imaging, albeit at the expense of reduced spatial resolution (notably axial resolution because of extended excitation PSF), it is prohibitive for STED microscopy. Indeed, beyond the NA limitation, the elimination of the marginal rays by the window design has a dramatic effect on the STED-PSF, rendering it useless, even counterproductive, for improving the STED axial resolution.

To further investigate this effect on the STED PSF and the resulting effective fluorescence PSF, we modified the calculation to consider the effect of the cranial window. We introduced an additional amplitude mask $T(\rho, \varphi)$ in Eq. (2), which models the additional aperture stop at the entrance of the window leading to the clipping of the outer rays after the objectives. The diffraction integral can be expressed as

$$\mathbf{E}(x, y, z) = C \int_0^\alpha \int_0^{2\pi} T(\theta, \varphi) \mathbf{B}(\theta, \varphi) \mathbf{P}(\theta, \varphi) e^{i(M(\theta, \varphi) + \Phi(\theta, \varphi))} e^{ik_0 n_1 (x \cos \varphi \sin \theta_1 + y \sin \varphi \sin \theta_1)} e^{ik_0 n_3 z \cos \theta_3} e^{ik_0 (n_3 d \cos \theta_3 - n_1 (t+d) \cos \theta_1)} \sin \theta d\theta d\varphi, \quad (11)$$

with

$$T(\theta) = \begin{cases} 1 & \text{for } \theta \leq \theta_c & \text{transmitted rays,} \\ 0 & \text{for } \theta_c < \theta \leq \alpha & \text{blocked region,} \end{cases} \quad (12)$$

where θ_c is the angle between the optical axis and the marginal ray of the cranial window on the output pupil of the objective.

Figures 2(b)–2(f) displays the results of these simulations. In Figs. 2(b) and 2(c), looking at the donut beam, the effect of the reduced NA is easily visible through a clear elongation of the profile. Yet, the presence of the cranial window does not change the geometry of the phase mask (it remains a vortex) and hence the symmetry of the PSF. Therefore, even if suboptimal, this configuration still permits superresolution imaging. In Fig. 2(d), in contrast, the bottle beam is dramatically degraded in the presence of the cranial window. In Fig. 2(e), in the case of the ring phase mask, the outer rays (with 0 phase—blue area in the phase mask) are not passing through the hippocampal window, whereas the inner rays (with π phase—red area in the phase mask) remain unaffected. This prevents destructive interference to happen in the focus and hence the formation of the central zero that is required for suppressing the fluorescence in the periphery of the fluorescence PSF while leaving the central region unaffected. In Fig. 2(e), note that by simply adjusting the ring radius on the phase mask, one could effectively retrieve a correct bottle beam profile. Yet, this does not solve the issue of the elongated shape [see panel (d) and (f)] due to the limited effective NA, which results in decreased axial resolution.

4.2 New Cranial Window Design and Experimental Validation

To retrieve a usable bottle beam and to achieve a substantial STED gain in spatial resolution in all three dimensions, we designed a new cranial window, or hippocampal porthole. Although increasing the radius of the conical window is possible [Fig. 3(a)], retrieving the full NA would require implanting a cylinder with a diameter of 5.1 mm into in the mouse brain, which is prohibitive in terms of the amount of cortical volume that would have to be surgically removed (about 45 mm³ of cortex). Instead, we chose to modify the geometry of the window. Using a conical shape [Fig. 3(b), see [Supplementary Fig. S1](#) (3D drawing)] makes it possible to benefit

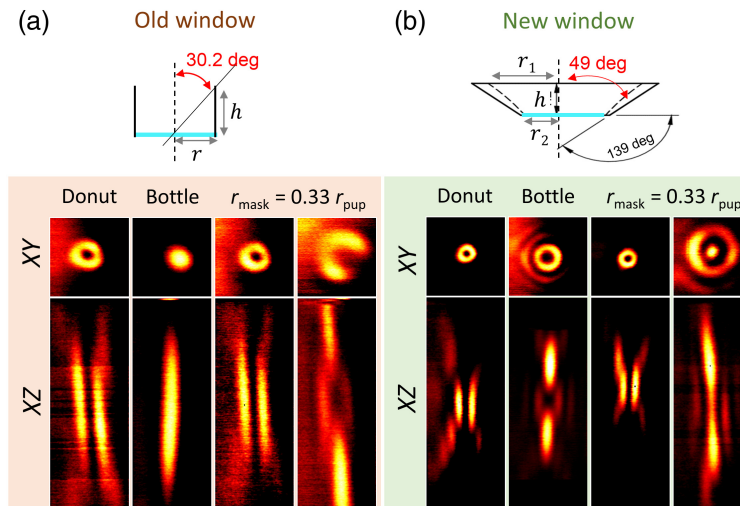


Fig. 3 Schematic of the (a) old and (b) new hippocampal windows (top panels). The conical shape makes it possible to use the full NA of the objective while minimizing the cortical volume that needs to be removed. STED beam PSFs (bottom panels) in XY ($2 \times 2 \mu\text{m}^2$) and XZ ($2 \times 8 \mu\text{m}^2$) planes experimentally measured, using gold nanoparticles attached to the coverslip, and imaged through the new (top panel) and old (bottom panel) cranial window designs, demonstrating the recovery of the appropriate bottle beam shape. In the right panels, the radius of the phase mask has been adjusted using the SLM.

from the full nominal NA of the objective, while minimizing the amount of tissue that needs to be resected to expose the hippocampus, reducing it to about 14 mm^3 , which is less than one third.

We first validated this cranial window geometry *ex vivo*, by placing gold nanoparticles on a poly-L-lysine coated coverslip, the same that we had used in the cranial window for *in vivo* imaging, and imaged them either through the cylinder (old window) or conical (new window) porthole without implantation on the head of the animal. This illustrates experimentally the impact of the cranial window design on the PSF of the STED beam.

Figure 3 clearly illustrates the effect of the two different cranial window designs on the STED PSF. Beyond the reduction of the NA, the old cylindrical window seriously degrades the shape of the bottle beam, obliterating the central intensity minimum, which is a must for STED microscopy. By contrast, the new conical cranial window design permits the generation of improved donut and bottle beam shapes. With the new design, the NA is limited by the optical design of the objective, and not the geometry of the optical access.

4.3 In Vivo 3D-STED Imaging in the Hippocampus

To visualize the gain in resolution in live conditions, fluorescence beads (diameter: $170 \mu\text{m}$) were attached to the coverslip using poly-L-lysine prior to be grafted into the animal. Imaging the fluorescent beads through the old and new window designs makes it possible to quantify and compare the gain in resolution between them. Figure 4 displays images in XY and XZ direction of the fluorescent beads visualized through the cranial window. Note that the look-up table is adjusted between images for better visualization.

Table 1 reports the axial and lateral resolution obtained experimentally using the two different windows together with the theoretical resolution obtained from numerical simulations. In this table, the spatial resolution is estimated as the full-width at half maximum (FWHM) of the PSF. Beyond the resolution, we quantified the maximum number of counts on the detector as a measure of image brightness (and thus SNR), which is strongly affected by the window geometry. Comparing our simulations with the experimental results, we normalized the number of counts in the simulated image with the value obtained from 2-photon images acquired with the new cranial window (which is expected to yield the highest number of counts).

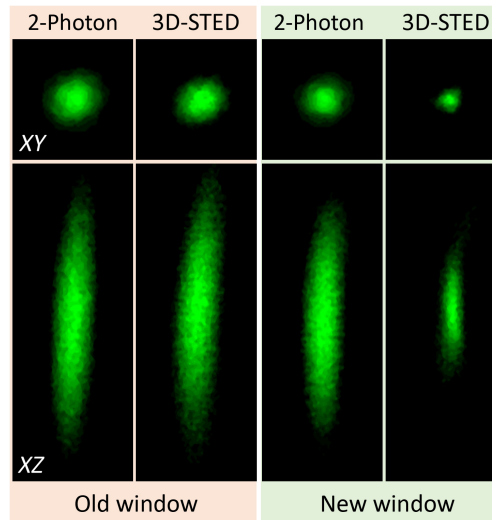


Fig. 4 Effective fluorescence PSF in 2-photon and 3D-STED obtained by imaging the fluorescent nanoparticles attached below the coverslip in the old cylindrical and new conical cranial window implanted above the hippocampus of an adult mice. *XY* image size: $1.5 \times 1.5 \mu\text{m}^2$ and *XZ* image size $1.5 \times 4 \mu\text{m}^2$.

Table 1 Spatial resolution (estimated as FWHM of the PSF) and maximum number of counts obtained in 2-photon and STED with the two different cranial window geometries. Mean \pm SD from 10 fluorescent beads in 2 different samples prepared from the same batch.

		XY resolution (nm)		Z resolution (nm)		I_{max} (No. of counts)	
		2-photon	STED	2-photon	STED	2-photon	STED
Cylindrical window	Simu	472	456	2831	2788	60	17
	Exp	470 ± 10	430 ± 20	2800 ± 150	2500 ± 500	50 ± 20	20 ± 15
Conical window	Simu	344	81	1244	285	158	138
	Exp	350 ± 8	80 ± 10	1200 ± 100	310 ± 40	158 ± 8	110 ± 10

The 2-photon PSFs are slightly improved by the new cylindrical window, yielding a modest but clear improvement in spatial resolution. In contrast, the 3D-STED performance is greatly affected by the type of window design. With the old cylindrical window, the effective PSF is very similar to the 2-photon PSF but with a strongly reduced signal, as expected from the absence of a zero in the bottle beam profile, diminishing the excitation of molecules without yielding of a gain in spatial resolution. In contrast, the new conical window permits a significant constriction of the fluorescent spot, while largely preserving the signal level.

Having established this proof of principle, we validated this modified hippocampal window on biological samples by imaging fluorescently labeled neurons in living transgenic mice. Figure 5(a) shows a segment of dendrite in the *Stratum radiatum* of the CA1 region in the hippocampus of a living mouse. Notably, the fine morphological features, including the hallmark cup-like shapes of spine heads and the ultrathin neck regions, connecting the spine head with the dendrite, can be appreciated with unprecedentedly high image quality in an *in vivo* setting. Figures 5(b) and 5(c) show a volume rendering of the same segment of dendrite qualitatively illustrating the gain in resolution and anatomical fidelity that can be achieved by our improved approach.

Finally, we also quantified neck diameters of the dendritic spines using a semiautomatic software,³⁹ which was specifically designed for morphometric analysis of superresolution images of dendritic spines. The results are summarized in Table 2 and are consistent with the published literature based on electron microscopy or STED imaging in brain slices.^{40–42}

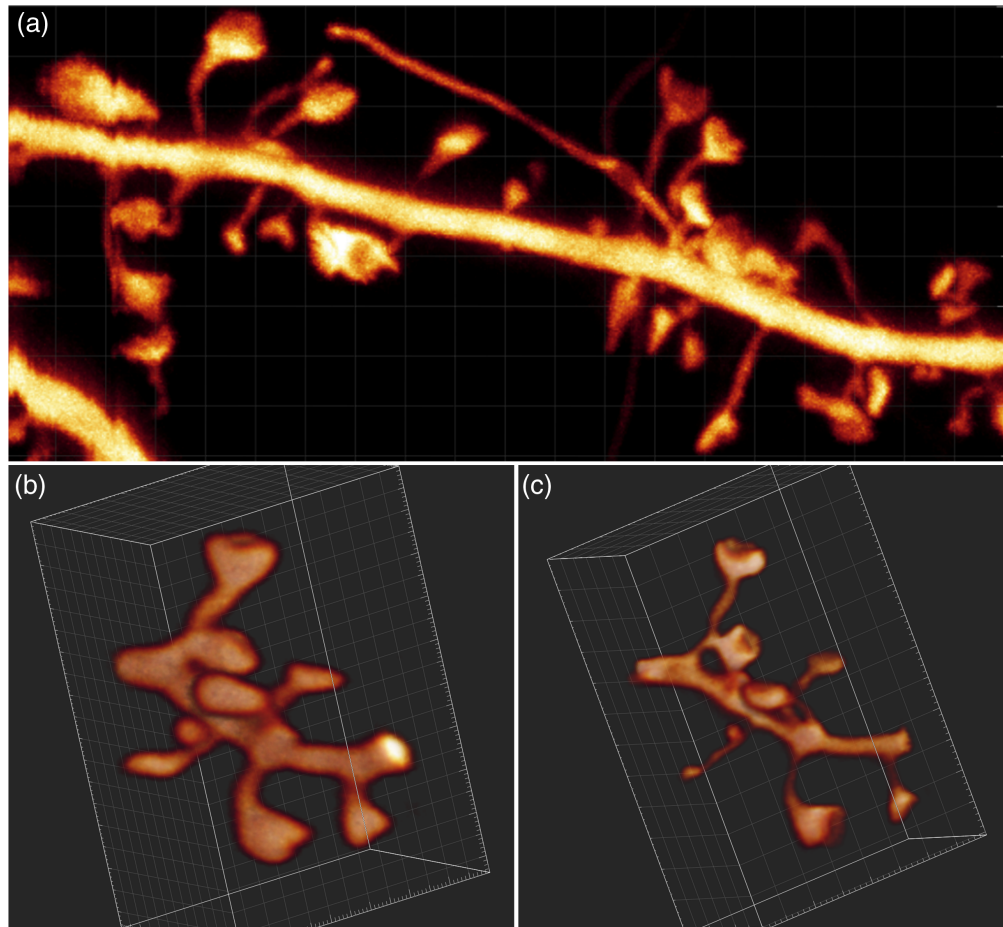


Fig. 5 (a) Image of a YFP-labeled segment dendrite in the *S. radiatum* of a Thy1 – $H^{tg/+}$ mouse, lying about 30 μm below the surgically created surface. Image size $5 \times 11 \mu\text{m}^2$. (b), (c) 3D rendering of the same segment of dendrite obtained with 2-photon and 3D-STED imaging, respectively. Image size $5 \times 3.2 \times 3.2 \mu\text{m}^3$. Panels (b) and (c) are still images from videos, 2-photon (Video 1) and STED (Video 2) (Video 1, MP4, 18 MB [URL: <https://doi.org/10.1117/1.NPh.10.4.044402.s1>]), (Video 2, MP4, 21 MB [URL: <https://doi.org/10.1117/1.NPh.10.4.044402.s2>]).

Table 2 Average spine morphological parameters measured by 2-photon and 3D-STED microscopy. Mean \pm SD from 23 spines collected from 3 mice.

	Spine neck with (μm)		Spine neck length (μm)	Spine head volume (μm^3)
	Lateral	Axial		
2-photon	0.45 ± 0.05	1.5 ± 0.4	0.7 ± 0.3	0.4 ± 0.2
3D-STED	0.17 ± 0.03	0.39 ± 0.08	0.8 ± 0.3	0.1 ± 0.1

5 Conclusion

In this paper, we propose and validate a modified hippocampal window design, which makes full use of the NA of a long-working distance objective. Although this new design by itself already increases the spatial resolution and optical sectioning of 2-photon microscopy, it is essential for STED microscopy. Notably, it can preserve the bottle beam shape needed for 3D-STED microscopy. We illustrate the benefit of this new cranial window design by visualizing dendritic spines, greatly improving STED image quality, rendering it comparable to the state of the art in brain slice preparations. Combined with state-of-the-art adaptive optics approaches,^{20,43}

this hippocampal window design will pave the way for 3D nanoscale imaging deep within the hippocampus of live mouse.

Our new approach improves the achievable spatial resolution for nanoscale imaging of neuro-anatomical structures and compartments (e.g., the extracellular space between brain cells^{44,45}), enabling longitudinal investigations into how their dynamics may underpin the ability of neurons and their networks to adapt themselves to ever-changing environmental conditions in health and disease.

Disclosures

The authors declare no conflict of interest.

Acknowledgments

This project received funding from the European Union's Horizon 2020 research and innovation program under the Marie Skłodowska-Curie action (Grant No. 794492), the Fonds AXA pour la Recherche to SB, the Doctoral School for Health and Life Sciences of the University of Bordeaux to JR, the European Research Council (ERC-SyG ENSEMBLE) (Grant No. 951294), Human Frontiers Science Program (Grant No. RGP0036/2020), ERA-NET NEURON (Grant No. ANR-17-NEU3-0005), the Fédération pour la recherche sur le cerveau (FRC), and Agence Nationale de la Recherche (Grant No. ANR-17-CE37-0011) to UVN. We thank the animal facility at IINS for their support.

Code, Data, and Availability

All datasets and codes are available from the corresponding authors upon reasonable request.

References

1. C. Sala and M. Segal, "Dendritic Spines: the locus of structural and functional plasticity," *Physiol. Rev.* **94**(1), 141–188 (2014).
2. R. Yuste and T. Bonhoeffer, "Genesis of dendritic spines: insights from ultrastructural and imaging studies," *Nat. Rev. Neurosci.* **5**(1), 24–34 (2004).
3. T. C. Südhof, "Neuroligins and neuroligins link synaptic function to cognitive disease," *Nature* **455**(7215), 903–911 (2008).
4. K. Svoboda and R. Yasuda, "Principles of two-photon excitation microscopy and its applications to neuroscience," *Neuron* **50**(6), 823–839 (2006).
5. Z. Mainen et al., "Two-photon imaging in living brain slices," *Methods* **18**(2), 231–239 (1999).
6. G. C. Ellis-Davies, "Two-photon microscopy for chemical neuroscience," *ACS Chem. Neurosci.* **2**(4), 185–197 (2011).
7. J. N. Kerr and W. Denk, "Imaging *in vivo*: watching the brain in action," *Nat. Rev. Neurosci.* **9**(3), 195–205 (2008).
8. M. J. Levene et al., "*In vivo* multiphoton microscopy of deep brain tissue," *J. Neurophysiol.* **91**(4), 1908–1912 (2004).
9. A. L. A. Mascaro, L. Sacconi, and F. S. Pavone, "Multi-photon nanosurgery in live brain," *Front. Neuroenergetics* **2**, 21 (2010).
10. A. Holtmaat and K. Svoboda, "Experience-dependent structural synaptic plasticity in the mammalian brain," *Nat. Rev. Neurosci.* **10**(9), 647–658 (2009).
11. J. T. Trachtenberg et al., "Long-term *in vivo* imaging of experience-dependent synaptic plasticity in adult cortex," *Nature* **420**(6917), 788–794 (2002).
12. S. K. Kim, K. Eto, and J. Nabekura, "Synaptic structure and function in the mouse somatosensory cortex during chronic pain: *in vivo* two-photon imaging," *Neural Plast.* **2012**, 640259 (2012).

13. S. El-Boustani et al., “Locally coordinated synaptic plasticity of visual cortex neurons *in vivo*,” *Science* **360**(6395), 1349–1354 (2018).
14. A. Mizrahi et al., “High-resolution *in vivo* imaging of hippocampal dendrites and spines,” *J. Neurosci.* **24**(13), 3147–3151 (2004).
15. L. Gu et al., “Long-term *in vivo* imaging of dendritic spines in the hippocampus reveals structural plasticity,” *J. Neurosci.* **34**(42), 13948–13953 (2014).
16. A. Attardo, J. E. Fitzgerald, and M. J. Schnitzer, “Impermanence of dendritic spines in live adult CA1 hippocampus,” *Nature* **523**(7562), 592–596 (2015).
17. S. W. Hell, “Far-field optical nanoscopy,” *Science* **316**(5828), 1153–1158 (2007).
18. S. Berning et al., “Nanoscopy in a living mouse brain,” *Science* **335**(6068), 551 (2012).
19. H. Steffens, W. Wegner, and K. I. Willig, “*In vivo* STED microscopy: a roadmap to nanoscale imaging in the living mouse,” *Methods* **174**, 42–48 (2020).
20. M. G. M. Velasco et al., “3D super-resolution deep-tissue imaging in living mice,” *Optica* **8**(4), 442–450 (2021).
21. K. I. Willig, “*In vivo* super-resolution of the brain—how to visualize the hidden nanoplasticity,” *iScience* **25**, 104961 (2022).
22. M. Fuhrmann et al., “Super-resolution microscopy opens new doors to life at the nanoscale,” *J. Neurosci.* **42**(45), 8488–8497 (2022).
23. T. Pfeiffer et al., “Chronic 2P-STED imaging reveals high turnover of dendritic spines in the hippocampus *in vivo*,” *eLife* **7**, e34700 (2018).
24. C. V. Middendorff et al., “Isotropic 3D nanoscopy based on single emitter switching,” *Opt. Express* **16**(25), 20774–20788 (2008).
25. D. Wildanger et al., “A compact STED microscope providing 3D nanoscale resolution,” *J. Microsc.* **236**(1), 35–43 (2009).
26. M. O. Lenz et al., “3-D stimulated emission depletion microscopy with programmable aberration correction,” *J. Biophotonics* **7**(1–2), 29–36 (2014).
27. S. Bancelin et al., “Aberration correction in stimulated emission depletion microscopy to increase imaging depth in living brain tissue,” *Neurophotonics* **8**(3), 035001 (2021).
28. J. Heine et al., “Three dimensional live-cell sted microscopy at increased depth using a water immersion objective,” *Rev. Sci. Instrum.* **89**(5), 053701 (2018).
29. S. W. Cramer et al., “Through the looking glass: a review of cranial window technology for optical access to the brain,” *J. Neurosci. Methods* **354**, 109100 (2021).
30. P. Bethge et al., “Two-photon excitation STED microscopy in two colors in acute brain slices,” *Biophys. J.* **104**(4), 778–785 (2013).
31. G. Feng et al., “Imaging neuronal subsets in transgenic mice expressing multiple spectral variants of GFP,” *Neuron* **28**(1), 41–51 (2000).
32. D. A. Dombeck et al., “Functional imaging of hippocampal place cells at cellular resolution during virtual navigation,” *Nat. Neurosci.* **13**(11), 1433–1440 (2010).
33. E. Wolf, “Electromagnetic diffraction in optical systems—I. An integral representation of the image field,” *Proc. R. Soc. Lond. Ser. A. Math. Phys. Sci.* **253**(1274), 349–357 (1959).
34. B. Richards and E. Wolf, “Electromagnetic diffraction in optical systems-II. Structure of the image field in an aplanatic system,” *Proc. R. Soc. Lond. Ser. A. Math. Phys. Sci.* **253**(1274), 358–379 (1959).
35. M. Gu, *Advanced Optical imaging Theory*, Vol. 75, Springer Science & Business Media (2000).
36. P. Török et al., “Electromagnetic diffraction of light focused through a planar interface between materials of mismatched refractive indices: an integral representation,” *JOSA A* **12**(2), 325–332 (1995).
37. P. Török and P. Varga, “Electromagnetic diffraction of light focused through a stratified medium,” *Appl. Opt.* **36**(11), 2305–2312 (1997).
38. K. Willig et al., “STED microscopy resolves nanoparticle assemblies,” *New J. Phys.* **8**(6), 106 (2006).
39. F. Levet et al., “SpineJ: a software tool for quantitative analysis of nanoscale spine morphology,” *Methods* **174**, 49–55 (2020).

40. K. Harris and J. Stevens, "Dendritic spines of CA 1 pyramidal cells in the rat hippocampus: serial electron microscopy with reference to their biophysical characteristics," *J. Neurosci.* **9**(8), 2982–2997 (2018).
41. J. I. Arellano et al., "Ultrastructure of dendritic spines: correlation between synaptic and spine morphologies," *Front. Neurosci.* **1**(1), 131–143 (2007).
42. J. Tønnesen et al., "Spine neck plasticity regulates compartmentalization of synapses," *Nat. Neurosci.* **17**(5), 678–685 (2014).
43. T. J. Gould et al., "Adaptive optics enables 3D STED microscopy in aberrating specimens," *Opt. Express* **20**(19), 20998–21009 (2012).
44. J. Tønnesen, V. K. Inavalli, and U. V. Nägerl, "Super-resolution imaging of the extracellular space in living brain tissue," *Cell* **172**(5), 1108–1121.e15 (2018).
45. S. Hrabetova et al., "Unveiling the extracellular space of the brain: from super-resolved microstructure to *in vivo* function," *J. Neurosci.* **38**(44), 9355–9363 (2018).

U. Valentin Nägerl is a professor of neuroscience and bioimaging at the University of Bordeaux, where he leads a research group and is in charge of the masters program in biophotonics and neurotechnology. He studied physics and pre-clinical medicine in Göttingen, got his PhD in neuroscience from UCLA in 2000, and worked as a postdoc at the Max Planck Institute of Neurobiology. His research focuses on the development and application of super-resolution imaging techniques to study the structure and function of the brain's micro-architecture including its extracellular spaces.

Biographies of the other authors are not available.